

Removing streak artifacts from ECG-gated reconstructions using deconvolution

Cyril Mory^{a,*}, Vincent Auvray^b, Bo Zhang^b, Michael Grass^c, Dirk Schäfer^c, Simon Rit^d,
Françoise Peyrin^{a,e}, Philippe Douek^f and Loïc Boussel^f

^aUniversité de Lyon, CREATIS, INSA-Lyon, Université Lyon 1, Villeurbanne Cedex, France

^bPhilips Research Medisys, Suresnes, France

^cPhilips Research, Röntgenstrasse, Hamburg, Germany

^dUniversité de Lyon, CREATIS, Lyon, France

^eX-ray Imaging Group, European Synchrotron, Radiation Facility, BP, Grenoble Cedex, France

^fUniversité de Lyon, CREATIS, INSA-Lyon, Université Lyon 1, Hospices Civils de Lyon, Lyon, France

Received 7 May 2013

Revised 8 November 2013

Accepted 9 January 2014

Abstract.

BACKGROUND: 4D cardiac computed tomography aims at reconstructing the beating heart from a series of 2D projections and the simultaneously acquired electrocardiogram. Each cardiac phase is reconstructed by exploiting the subset of projections acquired during this particular cardiac phase only. In these conditions, the Feldkamp, Davis and Kress method (FDK) generates large streak artifacts in the reconstructed volumes, hampering the medical interpretation. These artifacts can be substantially reduced by deconvolution methods.

OBJECTIVE: The aim of this paper is to compare two 4D cardiac CT reconstruction methods based on deconvolution, and to evaluate their practical benefits on two applications: cardiac micro CT and human cardiac C-arm CT.

METHODS: The first evaluated method builds upon inverse filtering. It has been proposed recently and demonstrated on 4D cardiac micro CT. The second one is an iterative deconvolution method, and turns out equivalent to an ECG-gated Iterative Filtered Back Projection (ECG-gated IFBP).

RESULTS: Results are presented on simulated data in 2D parallel beam, 2D fan beam and 3D cone beam geometries.

CONCLUSIONS: Both methods are efficient on the cardiac micro CT simulations, but insufficient to handle 4D human cardiac C-Arm CT simulations. Overall, ECG-gated IFBP largely outperforms the inverse filtering method.

Keywords: C-Arm, computed tomography, cardiac, electrocardiogram, 4D, deconvolution, iterative FBP, inverse filtering, micro CT

1. Introduction

In the context of acute and chronic coronary artery disease, it would be of great clinical interest to obtain a 4D representation of the myocardium directly from a C-arm system in the interventional lab. The main challenge is to avoid the blurring induced by the cardiac motion. The reconstruction

*Corresponding author: Cyril Mory, Université de Lyon, CREATIS; CNRS UMR5220; Inserm U1044; INSA-Lyon; Université Lyon 1; F-69621 Villeurbanne Cedex, France. Tel.: +33 472 357 412; E-mail: cyril.mory@philips.com.

must be performed with specific algorithms, which rely on the patient's electrocardiogram (ECG) [1] or on a similar signal extracted from the projection data itself [2]. These algorithms usually select the projections where the heart is in a given motion state and discard the others. While it relies on a subset of data that has the advantage of being free of cardiac motion, this approach, called "retrospective gating", drastically reduces the number of available projections and creates gaps in their angular distribution. It leads to an ill-posed reconstruction problem where traditional FDK [3] gives disappointing results: the reconstructed images are corrupted by streak artifacts, which hamper the medical interpretation (See Fig. 7).

In order to generate streak-free reconstructions, several classes of methods have been proposed. Motion compensated reconstructions [4–8] attempt to estimate the motion of the heart, and take it into account in the reconstruction process. They highly depend on the accuracy of the motion estimation, which is very hard to perform on ECG-gated reconstructions because of streaks. Methods derived from the compressed sensing theory [9–16] compensate the loss of information caused by ECG-gating by introducing sparsity-based regularization priors in the solution. Although they exhibit impressive results, they prove difficult to tune when the goal is to preserve low contrast structures. In the case of 4D cardiac C-arm CT, the risk is high to artificially remove small regions that have a high clinical interest, for example early perfusion defects caused by myocardial infarction. A third class of methods performs an ECG-gated reconstruction (filtered back projection, short FBP, or algebraic reconstruction technique, short ART), and then attempts to filter out the streak artifacts using a deconvolution scheme. Several such methods have been proposed in the 1980's [17,18]. They have been recently reintroduced by Badea et al. in the context of 4D micro-CT [19]. Badea's method is simple to implement, fast, has only one parameter, and gives satisfying results on 4D cardiac micro CT in the mouse.

The aim of this paper is to compare the method proposed in [19] with one based on convex optimization, and equivalent to ECG-gated Iterative Filtered Back Projection (IFBP) [20–23]. The performances of the methods are evaluated on cardiac micro CT and human cardiac C-Arm CT simulations. ECG-gated IFBP has the advantage of being theoretically suited not only to parallel beam geometry (like [19] is), but also to fan beam and cone beam, which are the geometries used in practice. The different methods are described in Section 2, results are presented and quantified in Section 3. Section 4 contains the discussion and conclusion.

2. Materials and methods

2.1. *Retrospectively gated reconstruction*

In cardiac CT, there are several ways to deal with the fact that the heart beats. One can just choose not to take it into account, and reconstruct the cardiac volume as if the heart had been static. The result is called an "ungated" reconstruction: the static structures like the rib cage and spine are well reconstructed, but the contours of the heart are not sharp, and the location of fine and highly contrasted objects like iodine-injected coronary arteries is imprecise.

One can also choose to acquire the data exactly the same way, and simultaneously record the ECG signal of the patient. In this case, one can perform either an ungated reconstruction, or a gated one. ECG-gating is based on the assumption that the contraction state of the heart depends only on the relative position between two successive R-peaks of the ECG. It consists in selecting the cardiac phase (the moment in the cardiac cycle) that one wants to reconstruct, and performing the reconstruction using only

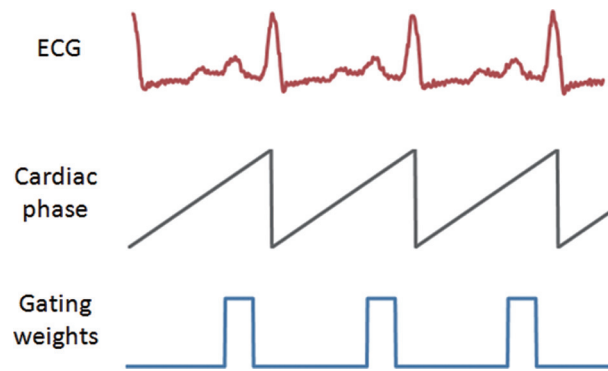


Fig. 1. This graph shows how ECG-gating is performed. A target cardiac phase is selected (here 80% of the distance between two peaks) and only the projections acquired during a cardiac phase close to the target are kept. The other ones are discarded. The ECG-gated dataset contains clusters of consecutive projections. (Colours are visible in the online version of the article; <http://dx.doi.org/10.3233/XST-140423>)

the projections acquired around this phase. This approach is called retrospective gating and is illustrated on Fig. 1. The methods presented in this paper build upon retrospective gating.

In the next subsection and throughout the paper, the following notations or their obvious extension to 3D will be used: the symbol $*$ denotes the convolution operator, and the symbol \times denotes the pointwise product, or the Cartesian product when used between sets. f is the object function from \mathbb{R}^2 to \mathbb{R} mapping the spatial coordinates (x, y) to the linear X-ray attenuation coefficients at that point. Let us define Θ the set of angles for which the projections are kept by ECG-gating. In practice, it gathers the projections belonging to the considered heart phase. The gating function g is defined by:

$$g : \mathbb{R} \times [0; \pi[\rightarrow \{0; 1\}$$

$$(r, \theta) \rightarrow \begin{cases} 0 & \text{if } r = 0 \\ 1 & \text{if } \theta \in \Theta \text{ and } r \neq 0 \\ 0 & \text{otherwise} \end{cases}$$

where (r, θ) are the usual polar coordinates.

The gated reconstruction can be written as $f_{\text{gated}} = \mathcal{R}^{-1}(g \times \mathcal{R}(f))$ where \mathcal{R} denotes the Radon transform and \mathcal{R}^{-1} the standard Filtered Back Projection [24]. Strictly speaking, \mathcal{R}^{-1} is really the inverse of \mathcal{R} only when no gating is performed, i.e. g is constant and equal to 1.

2.2. Parallel-beam gated reconstruction: a convolution procedure

For whatever subset Θ of $[0; \pi[$, the parallel-beam gated reconstruction process is a convolution. A rigorous proof can be derived from the Fourier Slice Theorem, but for the purpose of this paper, it is sufficient to note that $\mathcal{R}^{-1}(g \times \mathcal{R}(\cdot))$ is linear (which is obvious, because both \mathcal{R}^{-1} and \mathcal{R} are linear) and shift-invariant. The latter is less obvious, because neither \mathcal{R}^{-1} nor \mathcal{R} is shift-invariant.

$\mathcal{R}^{-1}(g \times \mathcal{R}(\cdot))$ is shift-invariant if and only if $\mathcal{R}_{\theta}^{-1}(\mathcal{R}_{\theta}(\cdot))$ is, where \mathcal{R}_{θ} and $\mathcal{R}_{\theta}^{-1}$ are respectively the projection and filtered back-projection along a single angle θ . It is a necessary condition because Θ can be chosen to contain only one angle, and a sufficient one because of linearity. In parallel beam, the single projection reconstructions of an image and of a shifted version of this image are just shifted

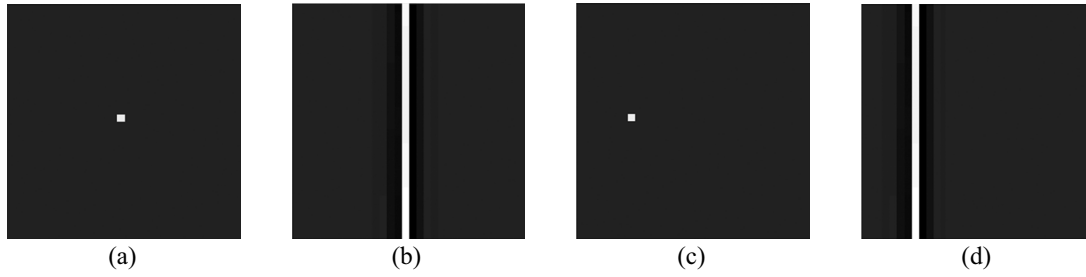


Fig. 2. Parallel beam case (a): Centered Dirac, (b): Reconstruction of (a) using only one projection, (c): Off-center Dirac, (d): Reconstruction of (c) using only one projection. For both reconstructions, the source is at the same location (under the image). (b) and (d) are shifted versions of one another.

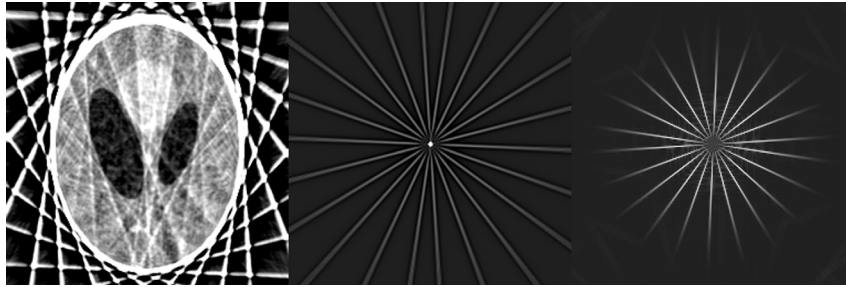


Fig. 3. From left to right, gated reconstruction of a phantom, gated reconstruction of a Dirac function (PSF of the gated reconstruction process), and shifted FFT of the Dirac peak's gated reconstruction. The streak pattern is the same on the Dirac and the phantom.

versions of one another, as illustrated on Fig. 2, and thus the parallel-beam gated reconstruction process is a convolution.

To recover f from f_{gated} , one can perform a deconvolution. The PSF is obtained by simply performing the gated reconstruction on a Dirac input (we call this gated reconstruction δ_{gated}). A typical PSF, and its 2D discrete Fourier transform, are plotted on Fig. 3, and the following relationship holds:

$$\mathcal{R}^{-1}(g \times \mathcal{R}(f)) = \delta_{\text{gated}} * f \quad (1)$$

It should be noted that some frequency information about the object function is lost during the gated reconstruction process (where $g(r, \theta)$ is 0 – see Fig. 3). This information will have to be extrapolated, explicitly or implicitly, in any deconvolution process.

2.3. Fan beam and cone beam geometries

In divergent beam geometry, the gated reconstruction process is linear, but not shift-invariant. To be more precise, in fan beam it is shift-invariant for very special cases of Θ , for example when $\Theta = \emptyset$ or $\Theta = [0; 2\pi[$, but not for most subsets of $[0; 2\pi[$ (see [25]). And in particular, $\mathcal{R}_{\theta}^{-1}(\mathcal{R}_{\theta}(\cdot))$ is not shift-invariant, as is illustrated on Fig. 4, which shows the single projection reconstructions of two Dirac functions, one centered, and the other one off-center. It is obvious that the reconstructions are not shifted version of one another. As a result, in the case of fan and cone beam projections, the gated FBP reconstruction process cannot be interpreted as a convolution.

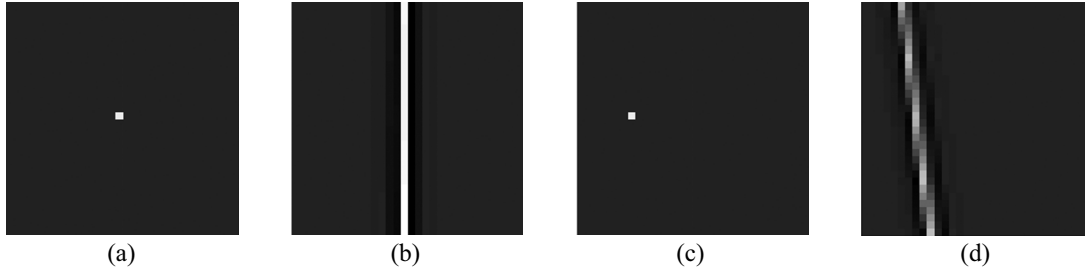


Fig. 4. Fan beam case (a): Centered Dirac, (b): Reconstruction of (a) using only one projection, (c): Off-center Dirac, (d): Reconstruction of (c) using only one projection. For both reconstructions, the source is at the same location (under the image). (b) and (d) are not shifted versions of one another.

2.4. Badea's method

A straightforward deconvolution method is called inverse filtering, and consists in dividing the Fourier transform of the convolved image f_c by the Fourier transform of the PSF, and applying an inverse Fourier transform on the result [26]. With \mathcal{F}_{2D} the 2D Fourier transform and \hat{f} the deconvolution result, inverse filtering is simply expressed as:

$$\mathcal{F}_{2D}(\hat{f})(u, v) = \frac{\mathcal{F}_{2D}(f_c)(u, v)}{\mathcal{F}_{2D}(\text{PSF})(u, v)} \quad (2)$$

The major problem is to handle the divisions by zero or almost zero, in particular when the Fourier transform of the PSF has many values close to zero (Fig. 3). It can lead to a strong amplification of the high frequency noise if improperly performed.

In [19], an important adaptation of inverse filtering was proposed to handle the zeros of the spectrum of the PSF. The voxel-by-voxel division in the Fourier domain is performed only when the magnitude of the Fourier coefficient of the PSF is above a certain threshold. In the other voxels, where $|\mathcal{F}_{2D}(\delta_{\text{gated}})(u, v)|$ is too close to zero, the division is considered unreliable and the corresponding Fourier coefficients are copied from the *ungated* reconstruction, which is the reconstruction obtained by taking into account the projections corresponding to all cardiac phases. This can be summarized as:

$$\mathcal{F}_{2D}(f)(u, v) = \begin{cases} \frac{\mathcal{F}_{2D}(f_{\text{gated}})(u, v)}{\mathcal{F}_{2D}(\delta_{\text{gated}})(u, v)} & \text{if } |\mathcal{F}_{2D}(\delta_{\text{gated}})(u, v)| > \text{threshold} \\ \mathcal{F}_{2D}(f_{\text{ungated}})(u, v) & \text{otherwise} \end{cases} \quad (3)$$

In practice, the images are reconstructed in a field of view twice as large as the object, and multiplied by a 2D cosine window, which helps mitigate the border effects. The threshold is set to 15% of the maximum value of $|\mathcal{F}_{2D}(\delta_{\text{gated}})|$, as recommended in [19].

2.5. Iterative methods

A straightforward iterative deconvolution method has been proposed by Van Cittert [27]. It can be applied to streak removal and leads naturally to iterative filtered back-projection.

In an attempt to iteratively deconvolve an image f_c , the Van Cittert method's update step is defined as follows:

$$f_{k+1} = f_k + \alpha(f_c - \text{PSF} * f_k) \quad (4)$$

where f_k is the deconvolved image at the k -th iteration, f_c is the observed image (here the gated reconstruction), and α a relaxation weight. Section 2.7 gives some insight on how to determine α .

This scheme is of particular interest, since it does not require explicit estimation of the PSF. One only needs to compute $\text{PSF} * f_k$, i.e. the forward projection of f_k , followed by a gated reconstruction, as stated in Eq. (1). An iterative method requires an initialization: the ungated reconstruction provides an excellent starting point in practice.

2.6. Iterative FDK

The update step of the Van Cittert method, modified as described in the previous subsection, is as follows:

$$f_{k+1} = f_k + \alpha (f_{\text{gated}} - \mathcal{R}^{-1}(g \times \mathcal{R}(f_k))) \quad (5)$$

$$f_{k+1} = f_k + \alpha (\mathcal{R}^{-1}(g \times \mathcal{R}(f)) - \mathcal{R}^{-1}(g \times \mathcal{R}(f_k))) \quad (6)$$

$$f_{k+1} = f_k + \alpha \mathcal{R}^{-1}(g \times (\mathcal{R}(f) - \mathcal{R}(f_k))) \quad (7)$$

Note that here, \mathcal{R} is not the exact Radon transform: it has a finite number of rays and projections, and can denote a forward projection in fan beam or cone beam geometry. It is called X-ray transform in the following. Also, whether an exact operator \mathcal{R}^{-1} exists or not depends on the trajectory [28], the beam geometry, the number of rays, projections, voxels, and on the spatial frequencies of the object [24]. Here \mathcal{R}^{-1} denotes the Filtered Back Projection (short FBP) in 2D, and the Feldkamp, Davis and Kress method (short FDK) in 3D.

Equation (7) means that a straightforward iterative deconvolution method to remove the streak artifacts consists in the following steps:

- Start from the ungated reconstruction.
- Until a stopping criterion is met.
 - * Forward project the current volume.
 - * Subtract the estimated projections from the measured ones.
 - * Apply the ECG gating to the subtracted data by selecting the projection angles inside the gating window.
 - * Apply an FBP or FDK to these “difference projections”.
 - * Add the result to the current volume (with a weight α).

For all the iterative FDK reconstructions presented in this paper, the parameter α was set to 0.02 and the number of iterations to 100. Setting a fixed number of iterations was the only stopping criterion.

This scheme can be interpreted as an iterative version of the Mc Kinnon – Bates algorithm [29]. It turns out that it has already been studied and is referred to as “Iterative Filtered Back Projection” (short IFBP). However, to the best of the authors’ knowledge, only ungated IFBP has been the topic of recent research, in order to remove cone beam or metal artifacts [20,21]. Limited view IFBP has been studied, but never exactly on the same problem: in [22], the authors study the so-called “bagel problem”, and in [23] the study is restricted to fan beam and uses iterative reconstruction-reprojection to estimate the missing views.

2.7. Convex optimization interpretation

The iterative scheme Eq. (7) does not model the streak removal process as a strict deconvolution problem, which allows relaxing the stationarity assumption. Thus, the method can be adapted to fan and cone-beam projections. This is justified by the following convex optimization interpretation of IFBP. The optimization perspective also helps understand how to set the parameter α . To this end, let us redefine the notations to fit into a linear algebra framework:

f is a column vector of size n , where n is the number of voxels. R is an $m \times n$ matrix, where m is the number of pixels in the projections dataset: it is the linear operator performing the X-ray transform. Its transpose R^T is the back projection operator. G is the ECG-gating matrix, of size $m \times m$. It is diagonal and binary. W is the ramp filtering operator, and is positive-definite. p_{measured} denotes the set of measured projections.

The ECG-gated reconstruction problem can be formulated as follows. The image f to be determined minimizes the following energy:

$$E(f) = \frac{1}{2} \left\| W^{\frac{1}{2}} G (p_{\text{measured}} - Rf) \right\|_2^2 \quad (8)$$

Note that without the W operator, $E(f)$ would be the energy minimized by ECG-gated ART. It would also be a valid approach for ECG-gated reconstruction. The aim here, though, is to give a convex optimization interpretation of IFBP, so ramp filtering needs to be performed. The gradient of this energy reads:

$$\nabla E(f) = R^T G^T W G (p_{\text{measured}} - Rf) \quad (9)$$

$$\nabla E(f) = R^T W G (p_{\text{measured}} - Rf) \quad (10)$$

because the ECG-gating and the ramp filtering commute (they can be performed in any order), and $G^T G = G$ because G is diagonal and binary. From Eq. (10), it is clear that a gradient descent procedure to find the minimum of this energy would have the following update step:

$$f_{k+1} = f_k + \alpha_k R^T W G (p_{\text{measured}} - Rf) \quad (11)$$

with α_k the gradient descent step at iteration k . Setting $\alpha_k = \alpha$ exactly boils down to the same update step as in Eq. (7). This proves that IFBP can be seen as a gradient descent to find the minimum of the energy defined in Eq. (8). The optimal value of the parameter α_k can be determined at each iteration: the problem was solved analytically by Lalush and Tsui in [30]. Other suboptimal, yet easier choices can be made ($\alpha_k = \alpha$, with a small fixed value, for example).

Additional constraints could easily be integrated into this framework, for example non-negativity.

2.8. Phantom generation

For the parallel beam and fan beam simulations the ‘‘modified Shepp and Logan’’ phantom generated by the ‘‘phantom’’ command in Matlab R2011a (The MathWorks Inc., Natick, MA, USA), with a size of 256*256 pixels, was used. One of the ellipses was set to change size with time, in order to simulate the beating motion of a heart. The systolic and diastolic phases are shown in Fig. 5, in the left and right column respectively, and the beating ellipse is pointed out by a red arrow.



Fig. 5. Shepp and Logan phantom with a beating ellipse, pointed out by a red arrow. The ground truth image for systole is shown on the left, the one for diastole is on the right. The display window is [0; 0.35].

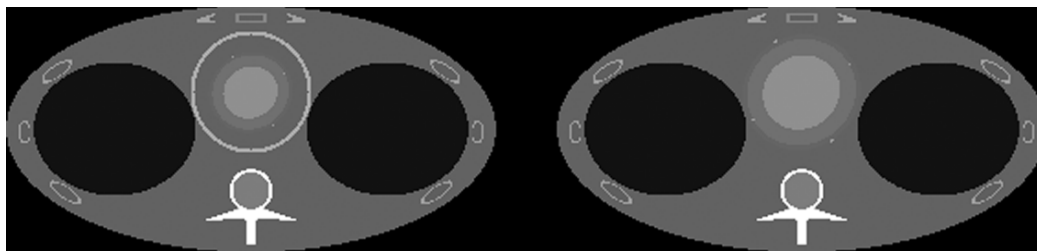


Fig. 6. Forbild phantom with a beating heart. On the left, the systolic state. On the right, the diastolic one. The red circle is the border of the ROI in which the local RMSE is computed. The display window is [0; 0.036].

In systole, in this slice, the beating ellipse's size is 26 pixels along the vertical direction and 22 pixels along the horizontal one. These sizes become 59 pixels and 53 pixels respectively in diastole.

For the cone beam simulations the phantom was a modification of the Forbild, into which a set of beating ellipses and tori were added to simulate a beating heart and coronary arteries [31]. Systole and diastole are represented in Fig. 6.

In systole, in this slice, the beating ellipse's size is 31 pixels along the vertical direction and 28 pixels along the horizontal one. These sizes become 42 pixels and 42 pixels respectively in diastole.

2.9. Relationship between streak artifacts, heart rate and motion blurring

2.9.1. Link between heart rate and image quality

In tomography with few views, the more regular the angular distribution of the projections, the better the reconstruction is. This topic is developed in [33], where the concept of "data incoherence" is introduced and discussed. In an ECG-gated dataset, this distribution consists in clusters of consecutive projections separated by large gaps in the angular sampling. The number of clusters of consecutive projections is the number of cardiac cycles that have occurred during the acquisition. It only depends on the acquisition duration and on the patient's heart rate.

As consecutive projections are very similar, each cluster brings only marginally more information than its central projection alone, and a dataset with many clusters of few projections is preferable to a dataset with few clusters of many projections. Therefore, a higher heart rate or a longer acquisition time makes the lack of data less acute, which results in less streak artifacts. This effect has already been

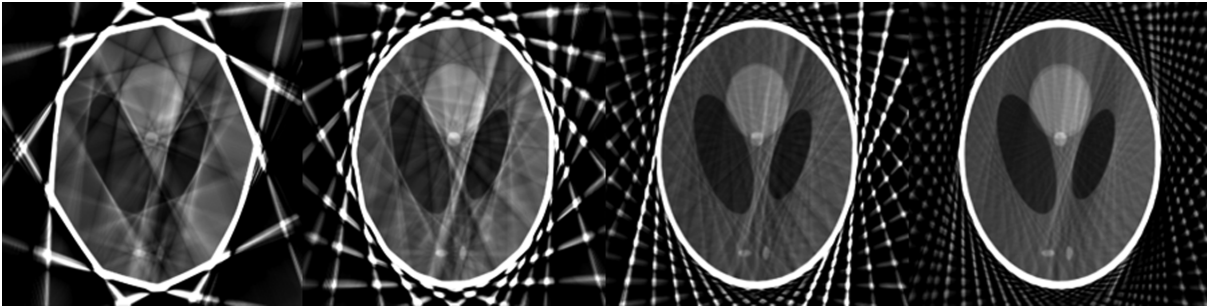


Fig. 7. FDK reconstructions of a Shepp and Logan phantom from 60 projections, grouped, from left to right, into 5, 10, 20 and 30 equally spaced clusters of 12, 6, 3 and 2 projections respectively.

documented [12,32] and is highlighted in Fig. 7, which shows ECG-gated FDK reconstructions of a Shepp and Logan phantom with different simulated heart rates. The full dataset is a simulated short scan of 300 projections over 10 seconds, and a 20% gating window is used, resulting in approximately 60 projections for each gated dataset. From left to right, the heart rates are 30, 60, 120 and 180 beats per minute, resulting in 5, 10, 20 and 30 equally spaced clusters of 12, 6, 3 and 2 projections respectively.

Note that very high heart rates can induce some blurring in the projections, because of the non-null detector integration time. This effect, however, is neglected in this paper.

2.9.2. Tradeoff between streak artifacts and motion blurring

As can be seen in Fig. 7, even for high heart rates, retrospectively ECG-gated reconstructions still contain streak artifacts. In many clinical situations, radiologists cannot make a diagnosis based on this kind of volumes: in the transverse plane, as in Fig. 7, the streak artifacts can usually be distinguished from the real structures, but the distinction is harder to make in the sagittal or coronal planes, and almost impossible on oblique cut planes, which are extensively used in cardiac imaging.

To mitigate the streak artifacts, most methods based on ECG-gating reinsert data from all cardiac phases at some point in the reconstruction process, which causes some blurring: in Badea's method, Fourier coefficients of the ungated FDK reconstruction are used during deconvolution; iterative methods, like SART [34] or iterative FDK, are initialized with the ungated FDK; even a compressed sensing method like PICCS [9,12] uses the ungated FDK as a prior. All these methods therefore imply a tradeoff between streak artifacts and motion blurring.

2.9.3. Conclusion

The type of artifacts caused by the lack of data depends on the specific reconstruction method: the ones presented in this paper lead to streaks, compressed sensing methods have over-regularization artifacts ("cartoon" effect for TV-regularization, Gibbs oscillations for Fourier-regularization), etc... A higher heart rate or a longer acquisition time imply a reduced amount of artifacts, which reduces the need for out-of-phase data and the motion blurring it induces, and overall leads to a better tradeoff.

2.10. Image quality metrics

Both Badea's method and iterative FDK imply a tradeoff between streak artifacts and motion blurring. Therefore quantitative measures of image quality must take into account both.

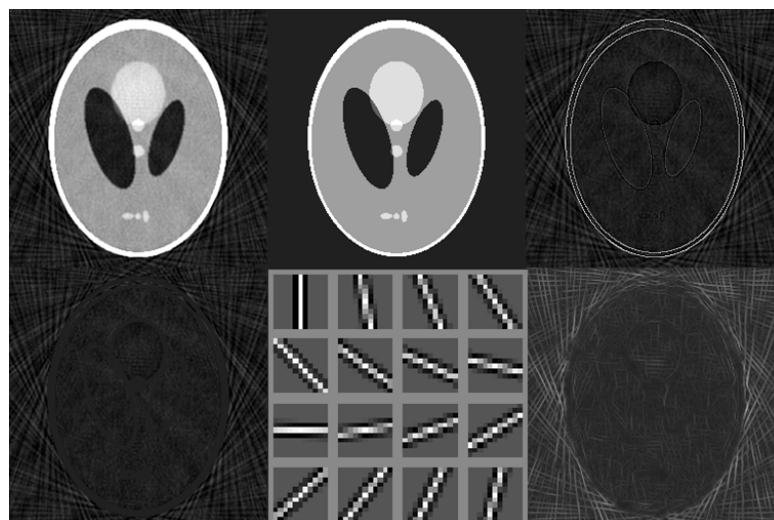


Fig. 8. Intermediate images in the streak index measurement process. The first row contains the input, the ground truth and their difference. The difference image has high values at the edges. Differences at these edge positions are removed (bottom left corner). The difference without edges is then convolved with a series of directional filters (bottom line, central column) and only the highest response for each pixel is kept (bottom right corner).

2.10.1. Sharpness

Visually, time resolution can be appreciated by looking at the shape and at the edges of the heart: the heart should be contracted in the systole reconstruction and dilated in the diastole reconstruction, and have sharp edges in both. Numerically, the similarity with the ideal shape is evaluated by computing a local root mean squared error (RMSE). In order to measure the sharpness of the edges of the beating ellipse, 17 profiles from the center of the ellipse to the outside have been extracted, and averaged into a single profile on which the 30%–70% amplitude distance has been measured [35]. The 30%–70% distance is the distance between the point where 30% of the amplitude of the edge has been reached, and the point where 70% of the amplitude of the edge has been reached. It was necessary to average a series of profiles to compute this metrics in order not to have it degraded by possible local streaks. This index proved consistent with the visual impression of sharpness.

On some ECG-gated FDK images, the streaks are so intense that they completely hide the edge, and no 30%–70% distance can be measured.

2.10.2. Streak artifacts quantification

For the quantification of streak artifacts it is proposed to isolate and highlight these artifacts in order to quantify them. The following procedure is carried out:

- Compute the difference between the image to be evaluated and the ground truth;
- Set the regions of this difference image to zero where the ground truth has edges (otherwise the small differences around the edges caused by interpolation would dominate in the metric). As a result, the difference image only contains streak artifacts and the texture of the noise;
- Detect and enhance the fine and elongated structures in this modified difference image by applying a simple ridgelet filter. This basic ridgelet filter consists in convolving the image with a series of directional high-pass filters, and keeping only the highest response for each pixel. This greatly mitigates the impact of the noise on the final measure;
- Compute the L1 norm of the output of the ridgelet filter.

Table 1
Numerical evaluation of parallel beam simulation results

Image		Global RMSE (mm^{-1})	Local RMSE (mm^{-1})	30%–70% distance (in pixels)	Streak index
Micro CT	Gated	111.1	27.8	2	16.83
	Ungated	59.9	50.9	10	0.76
	Badea	54.9	22.5	3	6.04
	IFBP	52.1	25.8	4	3.24
Human C Arm CT	Gated	228.9	49.6	2	34.46
	Ungated	60	49.5	10	1.15
	Badea	58.3	40.9	13	4.81
	IFBP	55.1	31.3	7	3.73

Table 2
Numerical evaluation of fan beam simulation results for a 20° fan angle

Image		Global RMSE (mm^{-1})	Local RMSE (mm^{-1})	30%–70% distance (in pixels)	Streak index
Micro CT	Gated	129.6	36.2	2	31.20
	Ungated	47.7	50.6	10	2.20
	Badea	93.2	31.1	4	15.13
	IFBP	40.3	24	4	4.06
Human C Arm CT	Gated	249.1	55.4	3	36.53
	Ungated	50.5	49.1	10	5.90
	Badea	84.3	41.4	9	10.72
	IFBP	47.1	34.3	8	7.07

The steps of this procedure are represented on Fig. 8. The result is a single index which measures the quantity of streaks contained in the image and, like the previous index, is consistent with visual image quality assessment.

3. Results

The simulation results for two different phantoms and two different sets of parameters are presented in the following. The experiments are carried out in parallel beam, fan beam and cone beam geometry.

Reconstructions are performed with four different methods: ECG-gated filtered back projection, ungated filtered back projection, deconvolution using Badea's method Eq. (3), and deconvolution using iterative filtered back projection Eq. (7). The ECG-gated filtered back projection images exhibit a good temporal resolution, but contain a lot of streak artifacts. The ungated filtered back projection images contain very little streak artifacts, but have no temporal resolution, since all cardiac phases are averaged. Badea's method and iterative filtered back projection both aim to obtain a compromise between streak artifacts and temporal resolution.

3.1. Numerical results

The numerical evaluations for parallel beam, 20° fan beam, 3D cone beam and noisy 3D cone beam are shown in Tables 1–4 respectively. They contain the following parameters:

- The root mean square error for the whole image (RMSE).
- The local RMSE for the region of interest containing the moving part of the phantom. For the Shepp and Logan phantom, this ROI is the beating ellipse in diastole, shown on Fig. 5. For the

Table 3
Numerical evaluation of cone beam simulation results

Image		Global RMSE (mm^{-1})	Local RMSE (mm^{-1})	30%–70% distance (in pixels)	Streak index
Micro CT	Gated	3.59	2.19	2	0.416
	Ungated	1.82	1.15	4	0.050
	Badea	3.01	1.58	2	0.401
	IFBP	2.00	1.00	2	0.188
Human C Arm CT	Gated	7.13	4.50	N/A	0.590
	Ungated	1.90	1.19	4	0.139
	Badea	3.38	1.72	2	0.277
	IFBP	1.93	1.05	2	0.148

Table 4
Numerical evaluation of noisy cone beam simulation results

Image		Global RMSE (mm^{-1})	Local RMSE (mm^{-1})	30%–70% distance (in pixels)	Streak index
Micro CT	Gated	3.80	2.45	3	0.539
	Ungated	1.95	1.30	4	0.200
	Badea	3.33	2.02	3	0.568
	IFBP	2.62	1.87	2	0.523
Human C Arm CT	Gated	7.46	4.80	N/A	0.878
	Ungated	2.22	1.50	4	0.353
	Badea	3.60	1.99	3	0.445
	IFBP	2.48	1.74	2	0.457

Forbild phantom, this ROI is shown on Fig. 6 by a red circle. To improve readability, the RMSE and local RMSE have been multiplied by 1000.

- The 30%–70% distance.
- The streak index.

Numerical evaluations of the cone beam data has been performed on the central slice.

As ECG-gated FDK reconstructions typically have inaccurate absolute attenuation values, even if proper reweighting of the projections is performed [36], they have been rescaled to obtain attenuation values that approximately match the ground truth. It should be kept in mind when interpreting the RMSE and local RMSE results of these images.

3.2. 2D parallel beam

Two different sets of parameters are used: the first one simulates the acquisition conditions of cardiac micro CT as described in [19], where instead of using a fixed high heart rate, the authors simulated it by randomly determining the phase through which each projection is computed; the second one simulates the acquisition conditions of human cardiac C-Arm CT:

- Micro CT settings: 1000 projections, each one containing 367 rays. Each projection is computed through a randomly determined phase (among 100 possible phases). For the gated reconstructions the projections computed through the 10 closest phases are used. Each gated reconstruction thus uses on average 100 randomly distributed projections,
- C-Arm CT settings: 300 projections, each one containing 367 rays. Each projection is computed through a phantom that beats at 60 bpm, during a 10 s simulated acquisition. For the gated reconstructions, a 10% gating window centered on the end-diastolic phase was used,

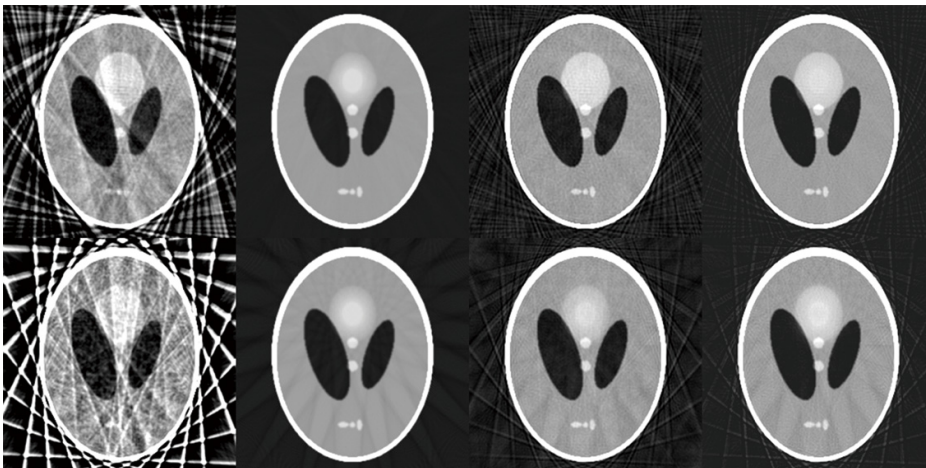


Fig. 9. Parallel beam reconstructions of the Shepp and Logan phantom with micro CT parameters (top row) and human cardiac C-Arm CT parameters (bottom row), with four different methods. From left to right: ECG-gated FBP, ungated FBP, deconvolution using Badea's method, iterative FBP deconvolution. The display window is $[0; 0.35]$.

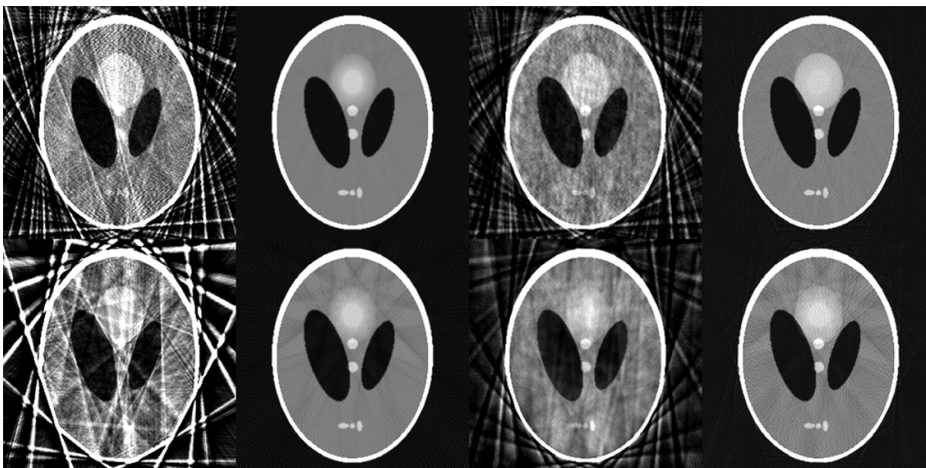


Fig. 10. Fan beam reconstructions of the Shepp and Logan phantom with micro CT parameters (top row) and human cardiac C-Arm CT parameters (bottom row), with 20° fan angle, and four different methods. From left to right: ECG-gated FBP, ungated FBP, deconvolution using Badea's method, iterative FBP deconvolution. The display window is $[0; 0.35]$.

- In both cases, a 180° source trajectory has been simulated and the projections were equally distributed over this angular range.

The results are presented in Fig. 9. Both Badea's method and iterative FBP efficiently remove the streaks from micro CT-like data, and generate image where the beating ellipse has sharp contours. Neither of them returns an image with a sharp beating ellipse using human C-Arm CT-like data acquisition.

3.3. 2D fan beam

Although Badea's method is theoretically not valid in fan beam geometry, it has been shown in [19] that it can still be used and have some efficiency in the case of a limited fan angle. The experiments in

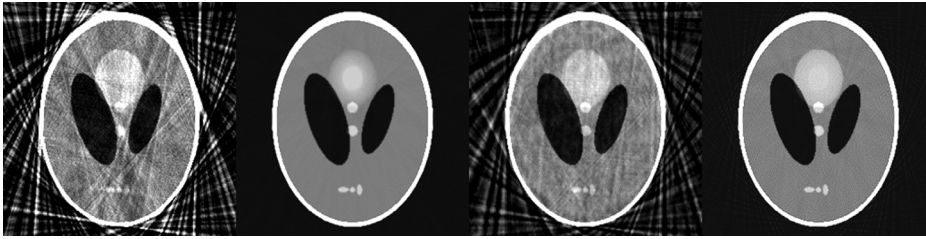


Fig. 11. Fan beam reconstructions of the Shepp and Logan phantom with micro CT parameters and a 6° fan angle. From left to right: ECG-gated FBP, ungated FBP, deconvolution using Badea's method, iterative FBP deconvolution. The display window is [0; 0.35].

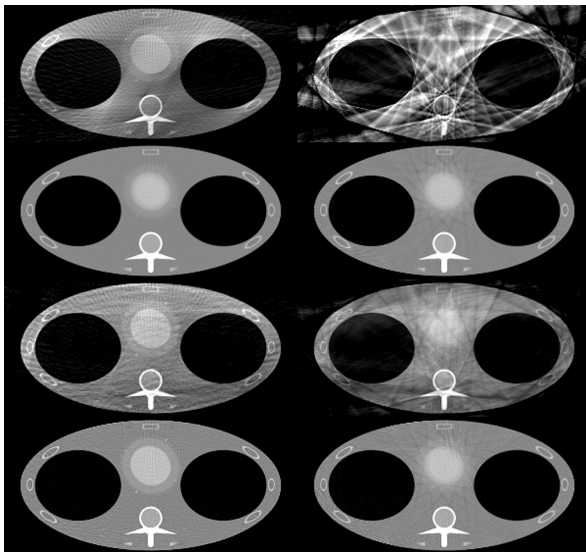


Fig. 12. Cone beam reconstructions of the modified Forbild phantom with micro CT parameters (left column) and human cardiac C-Arm CT parameters (right column), with four different methods. From top to bottom: ECG-gated FDK, ungated FDK, deconvolution using Badea's method, iterative FDK deconvolution. The display window is [0.005, 0.03].

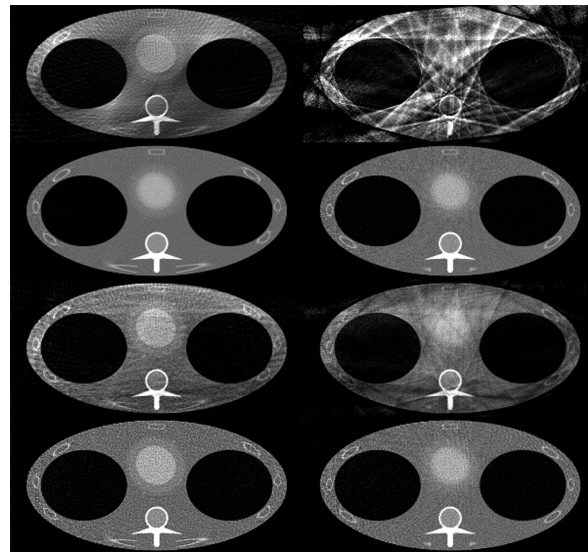


Fig. 13. Cone beam reconstructions of the noisy modified Forbild phantom with micro CT parameters (left column) and human cardiac C-Arm CT parameters (right column), with four different methods. From top to bottom: ECG-gated FDK, ungated FDK, deconvolution using Badea's method, iterative FDK deconvolution. The display window is [0.005, 0.03].

fan beam have been performed on the same phantoms and with the same parameters as for parallel beam. We present them for a 20° fan angle, which is close to a real C-Arm's fan angle. The source trajectory covered 360° , which explains the larger gaps in the angular sampling than in parallel beam geometry. The results are shown in Fig. 10. Both Badea's method and the iterative FBP generate images where the beating ellipse has sharp edges in the cardiac micro CT case, and images where the beating ellipse has poorly defined edges in the human cardiac C-Arm CT case. In addition, iterative FBP consistently shows fewer streaks than Badea's method.

In Badea's article it is shown that in low fan angle conditions their method, although theoretically not valid, can be used and generate satisfactory results. In Fig. 11, we compare Badea's method and IFBP for the reconstruction of the Micro-CT case. Even with a 6° fan angle, IFBP performs much better than Badea.

3.4. 3D cone beam

In order to perform the experiments in cone beam geometry, a modification of the 3D Forbild phantom [31,37] was used. It was animated to simulate a beating heart. The simulated projections were generated using the analytical version of the Forbild phantom. It was reconstructed as a $300 \times 128 \times 140$ voxels volume. Like in the 2D case, two different sets of parameters were used:

- Micro CT settings: 1000 projections of size 500×300 . This time, the phantom was set to beat at 600 bpm [19] instead of using a randomly chosen phase for each projection.
- C-Arm CT settings: 300 projections of size 500×300 computed through a phantom that beats at 60 bpm.
- The source trajectory covered 240° in 10 s, which is close to a real C-Arm acquisition. In both cases, the projections were equally distributed over this angular range.

In both cases, for the gated reconstructions, the gating window width was set to 10% of the cardiac cycle, centered on the end-diastolic phase.

Figure 12 shows the central slice of each volume. Note that even though it seems redundant with the fan beam study, because the central slice of a cone beam FDK is a fan beam FBP, it is not: in Badea's method, a 3D volume is deconvolved with a 3D PSF, thus the results are sensitive to cone beam-specific artifacts existing outside the central slice.

3.5. 3D cone beam with simulated noise

The same simulations and evaluations were carried out on noisy data. An additive white Gaussian noise of standard deviation 0.001 and mean 0 was added to the Forbild projections used in Section 3.4. The results are shown in Fig. 13. They are consistent with the noiseless results.

4. Discussion and conclusion

In the following, the main results of the simulation studies presented in this paper are discussed and briefly summarized. A conclusion with respect to iterative deconvolution methods and their applicability to ECG gated C-arm CT is given at the end of this section.

4.1. Comparison between Badea's method and iterative FBP

This work confirms that the streak removal method proposed in [19] performs well in the micro CT case. However the ECG-gated iterative FBP, which is theoretically better suited to approach the problem in divergent beam geometry, achieves a higher image quality in almost every simulation (Badea's method only performs marginally better than iterative FDK on local RMSE and 30%–70% distance in the micro CT parallel beam case, and on streak index in the noisy human C-arm CT cone beam case). Its iterative nature makes it slower than Badea's method, thus iterative FBP should be preferred when processing time is not an issue. Deconvolution by the iterative FBP method should be tested on real data to evaluate its performance in the presence of non-idealities of the acquisition system.

4.2. Impact of the angular distribution of projections on image quality

It has been shown that the angular distribution of the gated projections is an important parameter for ECG-gated reconstruction, and that this angular distribution is determined by the patient's cardiac rhythm and the rotation duration of the X-ray system. The faster the heart beats, the better the gated projections are distributed around the patient, and the better the image quality. The influence of the angular distribution is strong and when possible, the acquisition should be designed to result in an angular distribution as close as possible to equally spaced single projections.

4.3. Applicability to human cardiac C-Arm CT

The results also show that both methods deliver limited image quality for human C-Arm CT-like data acquisitions. The typical acquisition time for a rotational run and normal cardiac rhythms make the ECG-gated dataset very difficult to reconstruct. A straightforward protocol adaptation would be to make the acquisition slower and longer in order to have a more densely sampled angular space. This could either be a slow short scan acquisition at reduced angular speed or the acquisition of multiple circular arcs at comparable speed [38,39]. However, both approaches raise practical questions like the duration of the patient's breath-hold, dose adaptation to avoid large X-ray radiation, as well as the amount of contrast to be injected for angiographic studies.

In summary, the problem of image reconstruction from incomplete data due to gated acquisitions remains challenging. Since physiological and system parameters usually dictate the amount and the distribution of the data, image reconstruction is the preferred approach to tackle this problem. Regularized iterative reconstruction methods and motion compensated reconstruction approaches are the focus areas for future research. Though iterative deconvolution methods as they are known today do deliver an image quality improvement for system acquisition parameters evaluated in this study, the increase in image quality is still limited.

Acknowledgements

This work was supported by the laboratory CREATIS (Lyon, France), the Claude Bernard University (Lyon, France), the Hospices Civils de Lyon (Lyon, France), and Philips Research.

Many thanks to Cristian T. Badea and Samuel Johnston for their reactivity and kindness in answering our questions.

References

- [1] M. Kachelriess and W.A. Kalender, Electrocardiogram-correlated image reconstruction from subsecond spiral computed tomography scans of the heart, *Medical Physics* **25** (1998), 2417.
- [2] M. Kachelriess, D.A. Sennst, W. Maxlmoser and W.A. Kalender, Kymogram detection and kymogram-correlated image reconstruction from subsecond spiral computed tomography scans of the heart, *Med Phys* **29** (2002), 1489–1503.
- [3] L.A. Feldkamp, L.C. Davis and J.W. Kress, Practical cone-beam algorithm, *J Opt Soc Am A* **1** (1984), 612–619.
- [4] U. van Stevendaal, J. von Berg, C. Lorenz and M. Grass, A motion-compensated scheme for helical cone-beam reconstruction in cardiac CT angiography, *Medical Physics* **35** (2008), 3239–3251.
- [5] M. Prümmer, J. Hornegger, G. Lauritsch, L. Wigström, E. Girard-Hughes and R. Fahrig, Cardiac C-arm CT: A unified framework for motion estimation and dynamic CT, *IEEE Trans Med Imaging* **28** (2009), 1836–1849.

- [6] C. Rohkohl, G. Lauritsch, L. Biller, M. Prümmer, J. Boese and J. Hornegger, Interventional 4D motion estimation and reconstruction of cardiac vasculature without motion periodicity assumption, *Medical Image Analysis* **14** (2010), 687–694.
- [7] A.A. Isola, M. Grass and W.J. Niessen, Fully automatic nonrigid registration-based local motion estimation for motion-corrected iterative cardiac CT reconstruction, *Med Phys* **37** (2010), 1093–1109.
- [8] M. Brehm, P. Paysan, M. Oelhafen, P. Kunz and M. Kachelrieß, Self-adapting cyclic registration for motion-compensated cone-beam CT in image-guided radiation therapy, *Med Phys* **39** (2012), 7603–7618.
- [9] G.H. Chen, J. Tang and S. Leng, Prior image constrained compressed sensing (PICCS), *Proc Soc Photo Opt Instrum Eng* **6856** (2008), 685618.
- [10] J. Song, Q.H. Liu, G.A. Johnson and C.T. Badea, Sparseness prior based iterative image reconstruction for retrospectively gated cardiac micro-CT, *Medical Physics* **34** (2007), 4476.
- [11] C. Mory, B. Zhang, V. Auvray, M. Grass, D. Schafer, F. Peyrin, S. Rit, P. Douek and L. Bussel, ECG-gated C-arm computed tomography using L1 regularization, *Signal Processing Conference (EUSIPCO), 2012 Proceedings of the 20th European* (2012), 2728–2732.
- [12] G.-H. Chen, P. Theriault-Lauzier, J. Tang, B. Nett, S. Leng, J. Zambelli, Z. Qi, N. Bevins, A. Raval, S. Reeder and H. Rowley, Time-resolved interventional cardiac C-arm cone-beam CT: An application of the PICCS algorithm, *Medical Imaging, IEEE Transactions on* **31** (2012), 907–923.
- [13] S. Sawall, J. Kuntz, M. Socher, M. Knaup, A. Hess, S. Bartling and M. Kachelrieß, Imaging of cardiac perfusion of free-breathing small animals using dynamic phase-correlated micro-CT, *Med Phys* **39** (2012), 7499–7506.
- [14] E.Y. Sidky and X. Pan, Image reconstruction in circular cone-beam computed tomography by constrained, total-variation minimization, *Physics in Medicine and Biology* **53** (2008), 4777–4807.
- [15] L. Ritschl, S. Sawall, M. Knaup, A. Hess and M. Kachelrieß, Iterative 4D cardiac micro-CT image reconstruction using an adaptive spatio-temporal sparsity prior, *Phys Med Biol* **57** (2012), 1517–1525.
- [16] L. Zeng, B. Liu, L. Liu and C. Xiang, A new iterative reconstruction algorithm for 2D exterior fan-beam CT, *Journal of X-Ray Science and Technology* **18** (2010), 267–277.
- [17] A.P. Dhawan, R.M. Rangayyan and R. Gordon, Image restoration by Wiener deconvolution in limited-view computed tomography, *Appl Opt* **24** (1985), 4013–4020.
- [18] R. Gordon and R.M. Rangayyan, Geometric deconvolution: A meta-algorithm for limited view computed tomography, *IEEE Transactions on Biomedical Engineering* **BME-30** (1983), 806–810.
- [19] C.T. Badea, S.M. Johnston, Y. Qi and G.A. Johnson, 4D micro-CT for cardiac and perfusion applications with view under sampling, *Phys Med Biol* **56** (2011), 3351–3369.
- [20] J. Sunnegårdh and P.-E. Danielsson, Regularized iterative weighted filtered backprojection for helical cone-beam CT, *Medical Physics* **35** (2008), 4173–4185.
- [21] J. Sunnegårdh, *Iterative Filtered Backprojection Methods for Helical Cone-Beam CT* (Linköping University), 2009.
- [22] B.P. Medoff, W.R. Brody, M. Nassi and A. Macovski, Iterative convolution backprojection algorithms for image reconstruction from limited data, *J Opt Soc Am* **73** (1983), 1493–1500.
- [23] M. Nassi, W.R. Brody, B.P. Medoff and A. Macovski, Iterative reconstruction-reprojection: An algorithm for limited data cardiac-computed tomography, *IEEE Trans Biomed Eng* **29** (1982), 333–341.
- [24] A. Kak and M. Slaney, *Principles of Computerized Tomographic Imaging* (IEEE Press), 1988.
- [25] G.T. Gullberg, The reconstruction of fan-beam data by filtering the back-projection, *Computer Graphics and Image Processing* **10** (1979), 30–47.
- [26] R.N. Bracewell, *Fourier analysis and imaging*, 2003.
- [27] P.H. Van Cittert, Zum einfluss der spaltbreite auf die intensitätsverteilung in spektrallinien. II, *Zeitschrift für Physik* **69** (1931), 298–308.
- [28] H.K. Tuy, An inversion formula for cone-beam reconstruction, *SIAM Journal on Applied Mathematics* **43** (1983), 546–552.
- [29] G.C. Mc Kinnon and R.H. Bates, Towards imaging the beating heart usefully with a conventional CT scanner, *IEEE Trans Biomed Eng* **28** (1981), 123–127.
- [30] D.S. Lalush and B.M.W. Tsui, Improving the convergence of iterative filtered backprojection algorithms, *Medical Physics* **21** (1994), 1283–1286.
- [31] R. Manzke, P. Koken, D. Hawkes and M. Grass, Helical cardiac cone beam CT reconstruction with large area detectors: a simulation study, *Phys Med Biol* **50** (2005), 1547–1568.
- [32] J.G. Schwartz, A.M. Neubauer, T.E. Fagan, N.J. Noordhoek, M. Grass and J.D. Carroll, Potential role of three-dimensional rotational angiography and C-arm CT for valvular repair and implantation, *Int J Cardiovasc Imaging* **27** (2011), 1205–1222.
- [33] S. Abbas, T. Lee, S. Shin, R. Lee and S. Cho, Effects of sparse sampling schemes on image quality in low-dose CT, *Medical Physics* **40** (2013), 111915.
- [34] A.H. Andersen and A.C. Kak, Simultaneous algebraic reconstruction technique (SART): A superior implementation of

- the art algorithm, *Ultrason Imaging* **6** (1984), 81–94.
- [35] S.W. Smith, *The scientist and engineer's guide to digital signal processing*, (San Diego, CA, USA: California Technical Publishing), 1997.
- [36] D. Schäfer, C. Meyer, R. Bullens, A. Saalbach and P. Eshuis, Limited angle C-arm tomography and segmentation for guidance of atrial fibrillation ablation procedures, *Medical Image Computing and Computer-Assisted Intervention–MICCAI 2012* (Springer) (2012), 634–641.
- [37] C.O. Schirra, C. Bontus, U. van Stevendaal, O. Dössel and M. Grass, Improvement of cardiac CT reconstruction using local motion vector fields, *Computerized Medical Imaging and Graphics* **33** (2009), 122–130.
- [38] Lauritsch, J. Boese, L. Wigström, H. Kemeth and R. Fahrig, Towards cardiac C-arm computed tomography, *IEEE Trans Med Imaging* **25** (2006), 922–934.
- [39] S.E.J. Armitage, S.I. Pollmann, S.A. Detombe and M. Drangova, Least-error projection sorting to optimize retrospectively gated cardiac micro-CT of free-breathing mice, *Med Phys* **39** (2012), 1452–1461.